



**Synthesis and Characterization of a New Family of Layered
 $Pb_xSn_{4-x}As_3$ Alloys**

Journal:	<i>Journal of Materials Chemistry C</i>
Manuscript ID	TC-ART-02-2021-000842.R2
Article Type:	Paper
Date Submitted by the Author:	23-Apr-2021
Complete List of Authors:	Koster, Karl; The Ohio State University, Department of Chemistry and Biochemistry Wang, Yaxian; The Ohio State University, Department of Materials Science and Engineering Scudder, Michael; The Ohio State University, Department of Chemistry and Biochemistry Moore, Curtis; The Ohio State University, Department of Chemistry and Biochemistry Windl, Wolfgang; The Ohio State University, Department of Materials Science and Engineering Goldberger, Joshua; The Ohio State University, Department of Chemistry and Biochemistry

ARTICLE

Synthesis and Characterization of a New Family of Layered $\text{Pb}_x\text{Sn}_{4-x}\text{As}_3$ Alloys

Received 00th January 20xx,
Accepted 00th January 20xx

Karl G. Koster,^a Yaxian Wang,^b Michael R. Scudder,^a Curtis E. Moore,^a Wolfgang Windl,^b Joshua E. Goldberger^{*a}

DOI: 10.1039/x0xx00000x

Layered two-dimensional (2D) materials have attracted considerable interest for their exotic and anisotropic electronic behavior. One such material, Sn_2As_3 , bears a structural similarity and elemental composition to two other Sn- and As-containing layered materials that have recently demonstrated axis-dependent conduction polarity: NaSn_2As_2 and NaSnAs . Here, a new family of Pb-alloyed $\text{Pb}_x\text{Sn}_{4-x}\text{As}_3$ crystals was synthesized and the axis-dependent electronic and thermoelectric properties were evaluated. Up to one full equivalent of Pb could be alloyed into $\text{Pb}_x\text{Sn}_{4-x}\text{As}_3$ ($0 < x < 1.06$) before phase separation occurred. We establish the structural changes and the trends in the Raman spectra with increasing Pb substitution. These materials all exhibit metallic temperature-dependent resistivities and positive thermopowers along the in-plane and cross-plane directions. The absence of axis-dependent conduction polarity in these SnAs-layered materials is consistent with theoretical predictions, and illustrates that precise control over the atomic and electronic structure and doping is essential for realizing this phenomenon in new materials.

Introduction

Layered intermetallic phases have received a tremendous amount of research focus due to the plethora of unique properties and phenomena that they exhibit. For instance, BaSn_2 has been shown to be a topological insulator¹ while layered material GeAs_2 along with other pnictogen-containing materials such as SrGa_2As_2 and CaGa_2P_2 ,³ have shown considerable promise for applications in thermoelectrics. Other layered Zintl phases, such as EuSn_2As_2 ,^{4,5} and EuSn_2P_2 ,⁶ have been recently discovered to be magnetic topological insulators that can host Dirac-like surface states. There are numerous layered Zintl phase compounds, including CaAlSi , BaGaGe , and SrGaSn , that have been discovered to host superconducting behaviour at < 10 K.^{7,8} Due to this host of unique properties in these materials, the continued discovery of novel layered intermetallics remains an important goal towards furthering our understanding of tailoring the exotic physical properties in these compounds.

It has been recently discovered that many layered tin-arsenide intermetallics, particularly single crystals of NaSn_2As_2 ,^{9,10} and NaSnAs ,¹¹ have axis-dependent conduction polarity. These materials simultaneously exhibit *n*-type (electron) conduction that dominates along the in-plane directions and *p*-type (hole) conduction that dominates along

the out-of-plane direction.¹² Both compounds are primarily comprised of puckered honeycomb SnAs layers. In NaSnAs , a semiconductor with a 0.64 eV band gap, this exotic conduction behaviour is a consequence of the valence band maximum having dominant p_z character which causes holes to dominate cross-plane transport, along with the conduction band minimum being predominantly Sn/As p_x/p_y character so that electrons dominate in-plane transport. In contrast, NaSn_2As_2 is a metal with 0.5 fewer electrons per SnAs layer. Because of that, the same p-orbitals now merge into a single band that oscillates around the Fermi level, resulting in a Fermi surface with dominant convex (concave) curvature perpendicular (parallel) to the k_z -direction and axis-dependent conduction polarity (or “goniopolarity”). Considering that almost all modern electronic-devices require the integration of *n*-type and *p*-type materials for functionality, this axis-dependent conduction polarity has been targeted for many exciting applications, such as transverse thermoelectric devices.^{13–15} Overall, the realization of axis-dependent conduction polarity in NaSnAs and NaSn_2As_2 , as well as the need to further improve their functionality, inspired us to explore whether other layered tin-arsenide compounds and their derivatives also exhibit this exotic behaviour. In particular, we investigated Sn_4As_3 , a compound with a 7-layer Sn:As:Sn:As:Sn:As:Sn repeating sequence, and its alloys with Pb at the Sn sites. Pb was chosen as an alloy element because it is isovalent with Sn and its larger size and additional electron density would facilitate the use of X-ray diffraction to evaluate changes in the crystal structure. Additionally, the Pb-As bonds in this compound are of interest due to the complete lack of known binary Pb-As compounds. PbP_7 is the only known binary lead pnictide¹⁶ and other Pb- and As- containing compounds

^a Department of Chemistry and Biochemistry, The Ohio State University, Columbus, OH 43210, USA

^b Department of Materials Science and Engineering, The Ohio State University, Columbus, OH 43210, USA

*Electronic Supplementary Information (ESI) available. CCDC 2063177. For ESI and crystallographic data in CIF or other electronic format see

DOI: 10.1039/x0xx00000x

generally contain an electropositive cation as seen in $K_5As_3Pb_3$ and $K_8NbPbAs_5$,^{17,18} with the exception of $Pb_2As_xP_{14-x}$.¹⁹

Here, we discover a new family of $Pb_xSn_{4-x}As_3$ compounds and fully characterize its structural and electronic properties. Both powder and single-crystal X-ray diffraction measurements show that Pb preferentially substitutes with the middle two Sn positions in each 7-layer sequence, which agrees with DFT results. The isovalent substitution of Pb for Sn on these atomic sites results in a uniform increase in lattice parameters and distinct trends in the Raman spectra. These compounds are all metallic with resistivities that increase with greater Pb substitution, which is consistent with the Nordheim rule.^{20–22} Seebeck measurements reveal *p*-type conduction both in-plane and cross-plane across the entire alloy series and are in close agreement with the values predicted from theory. This work highlights the possibility of creating new Pb-containing layered materials and manipulating their electronic behaviour via alloying.

Experimental

Synthesis

Due to the extreme toxicity and volatility of Pb and As, all synthetic steps were performed in a glovebox. To synthesize crystals of Sn_4As_3 and the related alloy series $Pb_xSn_{4-x}As_3$, stoichiometric quantities of Pb (99.9%, Strem Chemicals), Sn (99.5%, Alfa Aesar), and As (99%, Strem Chemicals) powders were weighed out inside an Ar-filled glovebox and placed into a quartz tube that was then evacuated to a pressure of ~80 mTorr. Then, the quartz tube was slowly heated in a muffle furnace to a temperature of 850°C over the course of 12 hours. After holding at 850°C for 12 hours, the furnace was cooled slowly back to room temperature over the course of 144 hours to facilitate crystal growth.

Once the tubes had cooled to room temperature, they were cracked open in a fume hood revealing button-like morphologies. These buttons were gently fractured to reveal large platelet-shaped crystals. The outer layers of these crystals were cleaved further along the 001 axis via mechanical exfoliation with Kapton tape, revealing flat, mirror-like faces. All compounds were confirmed to be air-stable with no apparent signatures of degradation over months.

Structural Characterization

Each crystalline sample was ground into a powder and analysed with flat plate powder X-ray diffraction (PXRD) using a Bruker D8 X-ray diffractometer operating with a sealed Cu X-ray tube operating at 40 kV and 40 mA. The X-ray diffraction pattern that was obtained experimentally was analysed and refined using the Rietveld refinement software GSAS-II.²³

X-ray fluorescence (XRF) spectroscopy was used to quantify the Pb:Sn molar ratio in each $Pb_xSn_{4-x}As_3$ crystal via comparison with Sn/PbCl₂ standards. Spectra were collected on an ARL QUANT'X EDXRF Analyzer with an excitation voltage of 50 kV and a collection energy range of 0–40 keV. The $Pb_xSn_{4-x}As_3$

stoichiometries stated in this paper were defined using these XRF measurements.

Single-crystal X-Ray Diffraction studies were performed on a sample of $Pb_{0.68}Sn_{3.32}As_3$ in order to accurately determine the relative elemental site occupancies. These studies were carried out on a Nonius Kappa diffractometer equipped with a Bruker APEX-II CCD and Mo K_{α} radiation ($\lambda = 0.71073 \text{ \AA}$). A 0.059 x 0.056 x 0.048 mm piece of a metallic silver block was mounted on a MiTeGen Micromount with clear enamel. Data were collected in a nitrogen gas stream at 300(2) K using ϕ and ω scans. Crystal-to-detector distance was 40 mm and exposure time was 5 seconds per frame using a scan width of 2.0°. Data collection was 100% complete to 25.00° in θ . A total of 7321 reflections were collected covering the indices $-5 \leq h \leq 5$, $-5 \leq k \leq 5$, $-51 \leq l \leq 51$. 510 reflections were found to be symmetry independent, with a R_{int} of 0.0495. Indexing and unit cell refinement indicated a trigonal, rhombohedral lattice. The space group was found to be $R\bar{3}m$. The data were integrated using the Bruker SAINT software program and scaled using the SADABS software program. Solution by direct methods (SHELXT)^{24,25} produced a complete phasing model for refinement. All atoms were refined anisotropically by full-matrix least-squares (SHELXL-2014).²⁶ Heavy atom disorder was freely refined on all Pb/Sn sites, to independently confirm the Pb:Sn stoichiometry. The Pb/Sn pairs were constrained to have the same positional and thermal parameters. CSD 2063177 contains the supplementary crystallographic data for this paper.

Polarization-dependent Raman spectroscopy was performed at room temperature on *c*-axis oriented crystals of $Pb_xSn_{4-x}As_3$ in a backscattering configuration using a Renishaw Invia Raman Spectrometer equipped with a charge-coupled device detector and a 785 nm laser illumination source. In polarized Raman measurements, a KRS-5 polarizer was installed in the instrument, and rotated to be either coincident with the polarization of the laser source (0°), or rotated by 90°. Spectra were collected with a laser power density of $3.60 \times 10^5 \text{ W cm}^{-2}$.

Energy Dispersive X-ray spectroscopy (EDX) mapping was conducted with a FEI Helios Nanolab 600 Dual Beam Focused Ion Beam / Scanning Electron Microscope (SEM). Elemental EDX mapping was performed using INCA EDX analysis software.

Electronic structure calculations

The electronic band structure of Sn_4As_3 and the energetics in $Pb_xSn_{4-x}As_3$ were calculated using density functional theory (DFT) as implemented in the Vienna Ab-initio Simulation Package (VASP)^{27,28} with projector augmented wave Perdew-Burke-Ernzerhof (PAW-PBE) potentials.^{29,30} The kinetic energy cutoff for plane waves was set to 360 eV and the Brillouin-zone integration was performed on a Γ -centred $12 \times 12 \times 4$ *k*-point mesh for the conventional cell. For band structures, experimental lattice parameters were fixed while the ions were relaxed until the forces on all atoms were less than $10^{-4} \text{ eV \AA}^{-1}$. After the atomic positions were relaxed, we increased the *k*-point density to $36 \times 36 \times 12$ for the conventional cell to calculate band energy with better accuracy for reciprocal space integration into BoltzTraP.³¹ The necessary derivatives were

then calculated on a Fast Fourier Transform grid 15 times as dense as the DFT mesh. To calculate the Seebeck coefficient tensors, the linear Boltzmann equation solver BoltzTraP was employed. For total energy calculations in $\text{Pb}_x\text{Sn}_{4-x}\text{As}_3$, dispersive interactions were included in the form of Grimme's DFT-D3 correction method³² and $1\times 1\times 1$, $2\times 2\times 1$, and $3\times 3\times 1$ supercells were fully relaxed to study Pb ordering effects.

Electronic transport

Temperature-dependent resistivity measurements were conducted along the in-plane directions of single crystals from the alloy series $\text{Pb}_x\text{Sn}_{4-x}\text{As}_3$ using a four-probe measurement technique within a Quantum Design 14 T Physical Properties Measurement System from 2 to 300K. Electrical contacts were made to the sample using Epoxy Technology H2OE silver epoxy that was cured at 135°C in a fume hood.

The Seebeck coefficients and resistivities of the two end-members, Sn_4As_3 , and $\text{Pb}_{1.06}\text{Sn}_{2.94}\text{As}_3$ alloy series were both measured along the in-plane and cross-plane directions from 80K to 300K in a Janis liquid nitrogen vacuum cryostat. A four-probe measurement geometry was used to measure sample resistance. To measure the thermopowers of these samples, an electrical current was passed through a 120Ω Omega strain gauge attached to one end of the sample to create a temperature gradient along the direction of the crystal being measured. Two type T thermocouples, one placed near the hot side of the sample and one placed near the cold side of the sample, measured the resulting temperature gradient and the Seebeck voltage created across the sample. As before, thermal and electrical contacts were attached to the surface of the sample with H2OE silver epoxy that was cured at 135°C in a fume hood.

Results and Discussion

Single crystals of Sn_4As_3 were grown from the melt using a conventional solid-state synthesis technique. Structural refinement of single-crystal and powder X-ray diffraction data confirmed that the material crystallizes into the $R\bar{3}m$ space group with $a=4.0865(3)\text{Å}$ and $c=36.045(1)\text{Å}$, which is in close agreement with previous reports.^{33,34} The rhombohedral $R\bar{3}m$ structure of Sn_4As_3 is composed of a series of 7-layer Sn:As:Sn:As:Sn:As:Sn "packets."³⁴ Four layers of Sn atoms alternate with 3 layers of As atoms to form each seven-layer packet (Fig. 1a). The atoms in the middle two Sn layers are in pseudo-octahedral coordination with the neighbouring As atoms (Sn-As 2.86 Å - 3.04 Å) while the outer Sn layers that make up the top and bottom layer of each packet are in trigonal pyramidal coordination with As (Sn-As 2.72 Å - 2.76 Å). In Sn_4As_3 , the Sn-Sn distances between neighbouring packets (3.25 Å) are smaller than those found in exfoliatable van der Waals compounds (such as NaSn_2As_2 and EuSn_2As_2 , 3.30-3.33 Å)^{4,9,10} indicating stronger interlayer bonding. Indeed, our calculated DFT adhesion energy with a value of 0.98 J/m² is 46% higher than the 0.67 J/m² that we calculate with the same method for the adhesion energy between Sn-layers in NaSn_2As_2 ,

which explains why we found Sn_4As_3 to be more difficult to exfoliate than NaSn_2As_2 . Thus, numerous attempts to mechanically exfoliate Sn_4As_3 to thicknesses <100 nm proved unsuccessful.

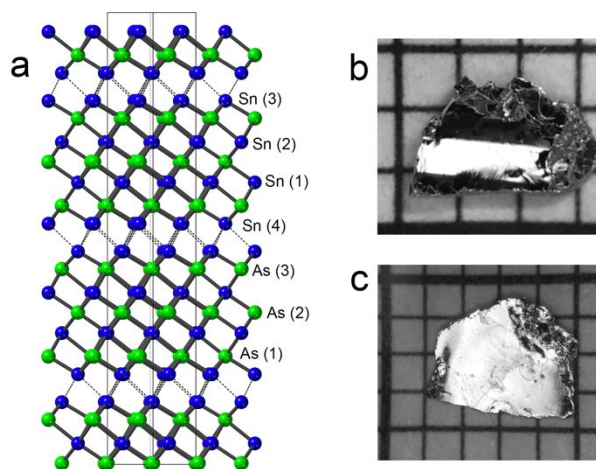


Figure 1: (a) The $R\bar{3}m$ layered structure of Sn_4As_3 , with blue spheres corresponding to Sn atoms and green spheres corresponding to As atoms. Single crystals of (b) Sn_4As_3 and (c) $\text{Pb}_{1.06}\text{Sn}_{2.94}\text{As}_3$ on 1 mm grid paper.

Up to approximately one fourth of the Sn atoms in Sn_4As_3 could be replaced by Pb atoms, allowing the formation of $\text{Pb}_x\text{Sn}_{4-x}\text{As}_3$ ($0 < x < 1.06$) alloys (Fig. 1b and 1c). Successful synthesis of these compounds was confirmed using powder X-ray diffraction and Rietveld refinement (Fig. 2a and 2b). As Pb was alloyed into Sn_4As_3 , the crystal structure transitioned from the trigonal non-centrosymmetric $R\bar{3}m$ space group to the centrosymmetric $R\bar{3}m$, as determined with single-crystal X-ray diffraction (Tables S1-S3, ESI[†]). Attempts to fit the single-crystal Pb-alloyed structure into the $R\bar{3}m$ space group resulted in a Flack parameter of ~ 0.3 , indicating partial twinning. When we refined the twinned structure using the TWIN/BASF command, the refinement could not converge. A much better fit and convergence were achieved assuming an $R\bar{3}m$ space group. The Pb content in each of these $\text{Pb}_x\text{Sn}_{4-x}\text{As}_3$ crystals was quantified using X-ray fluorescence spectroscopy (Fig. S1, ESI[†]). The increased full width at half maximum of the diffraction reflections upon incorporation of Pb in Fig. 2b indicates there is some variation in local Pb:Sn distribution in each alloy.

A uniform expansion in lattice parameters was observed with increasing Pb substitution via Rietveld refinement of the powder diffraction data (Fig. 2c and 2d). This is a direct result of the larger Pb atoms replacing slightly smaller Sn atoms in the crystal structure. Substitution of 1.06 equivalents of Pb into the Sn_4As_3 structure to form $\text{Pb}_{1.06}\text{Sn}_{2.94}\text{As}_3$ increases the c lattice parameter by 1.33% from $c = 36.0468(4)\text{Å}$ to $c = 36.5268(15)\text{Å}$, while the a lattice parameter increases by only 0.37% from $a = 4.0865(1)\text{Å}$ to $a = 4.1017(3)\text{Å}$. A linear and uniform increase in both lattice parameters is observed with greater Pb substitution across the alloy series, which is consistent with Vegard's law^{35,36} and suggests homogeneous alloy formation. Further and even stronger evidence for that is the excellent agreement with DFT

lattice parameters for Pb randomly substituted in the middle-two Sn layers, which are also shown in Fig. 2c. Given that Pb has a higher form factor than Sn, diffraction peak intensity generally increases across the $\text{Pb}_x\text{Sn}_{4-x}\text{As}_3$ alloy series as more Pb is alloyed into the Sn_4As_3 crystal structure. This effect is most pronounced at lower values of 2θ .

SEM microscopy coupled with EDX spectroscopy also confirmed that all three elements (Pb, Sn, and As) were distributed relatively homogeneously throughout the single crystals. No regions were found containing large excesses of Pb or Sn (Fig. S2, ESI[†]). Further attempts to increase the stoichiometry of Pb substitution beyond $x > 1$ resulted in the formation of a Pb impurity phase from the diffraction pattern.

In the non-centrosymmetric $R\bar{3}m$ crystal structure of Sn_4As_3 , there are 4 distinct Sn sites and 3 distinct As sites (Fig. 1). Sn sites 1 and 2 comprise the inner two Sn layers of each 7-layer packet while Sn sites 3 and 4 make up the outer two Sn layers of each packet. Additionally, As sites 1, 2, and 3 each represent individual As layers in the crystal structure. When Pb is alloyed into the Sn_4As_3 crystal structure to form the $\text{Pb}_x\text{Sn}_{4-x}\text{As}_3$ alloy series, the non-centrosymmetric $R\bar{3}m$ crystal structure transitions to a centrosymmetric $R\bar{3}m$ crystal structure. As a result, the two inner Sn sites (Sn 1 and 2 in $R\bar{3}m$) become equivalent, which we refer to as Sn(2) in $R\bar{3}m$. The two outer Sn sites (3 and 4) also become equivalent, which we label as Sn(1) in $R\bar{3}m$. As(1) and As(3) also become equivalent (As(1)) while As(2) has no equivalent atoms and is still labelled as As(2).

In the centrosymmetric $R\bar{3}m$ crystal structure of $\text{Pb}_x\text{Sn}_{4-x}\text{As}_3$, there are two possible Sn (6c) Wyckoff sites which Pb can possibly occupy in the Sn_4As_3 structure: the outer Sn(1) layer or the inner Sn(2) layer. To determine which atomic sites Pb atoms occupy when Pb is alloyed into the Sn_4As_3 structure, we analysed a crystal selected from the $\text{Pb}_{0.76}\text{Sn}_{3.24}\text{As}_3$ synthesis with single-crystal X-ray diffraction (Tables S1-S3, ESI[†]). When refining this single-crystal structure, the Pb:Sn site occupancy of each position was allowed to vary without restraints. Here, it was found that Pb preferentially occupies the inner Sn site (2) with minimal Pb on the outer Sn site (1). Completely removing Pb from the outer Sn site significantly improved the fit. This crystal refined to a stoichiometry of $\text{Pb}_{0.68}\text{Sn}_{3.32}\text{As}_3$, indicating that Pb content of individual crystals can vary from the overall stoichiometry of the synthesis.

We further confirmed this preferential site ordering by performing Rietveld refinements on a powder X-ray diffraction pattern of $\text{Pb}_{1.06}\text{Sn}_{3.24}\text{As}_3$, the most Pb-rich compound in the alloy series. We started by refining the Pb occupancy on Sn site 1, Sn site 2, or on both sites simultaneously. The best fit was achieved when Pb substituted with Sn exclusively within the two inner layers (site 2) of the seven-layer packet. Substituting Pb on the two outer layers (site 1) yielded a much worse fit. When the Pb-Sn occupancies of both sites were allowed to vary, Pb in the outer Sn site (1) was almost completely removed, further confirming the preference for Pb substitution in the middle two Sn layers (site 2). This is consistent with DFT results in which a Pb atom was moved from one of the inner layers (2) to an outer layer (1) in a $3 \times 3 \times 1$ supercell, resulting in an energy penalty of 0.14 eV, more than 40% higher than $k_B T$ at any of the

processing temperatures. In the final Rietveld refinements of the powder diffraction patterns of $\text{Pb}_x\text{Sn}_{4-x}\text{As}_3$, the total Pb occupancy in the compound was fixed to the value determined with X-ray fluorescence spectroscopy and was distributed exclusively on the inner Sn(2) site. These refined structures are shown in Tables S4-S13 (ESI[†]). Finally, these PXRD refinements indicate that Sn_4As_3 and its Pb-alloyed derivatives all show a significant lone pair distortion with the central two Sn/Pb-As bonds being 0.14-0.25 Å shorter than the bonds between the inner Sn atoms and the outer As atoms (Fig. S3, ESI[†]). Similar bond length asymmetries were observed in DFT calculations (Fig. S4, ESI[†]).

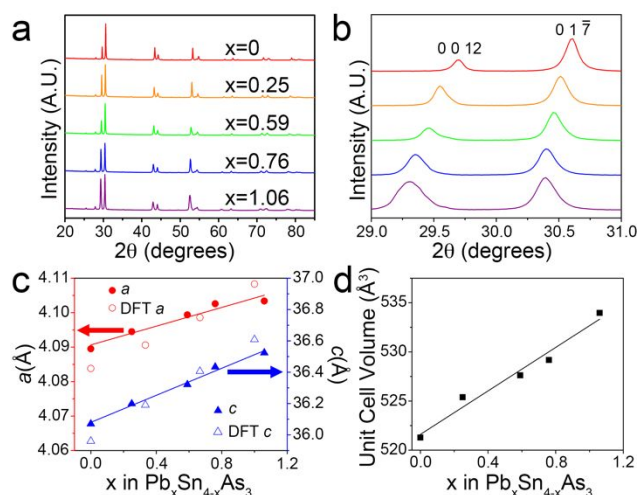


Figure 2: (a) PXRD patterns for $\text{Pb}_x\text{Sn}_{4-x}\text{As}_3$ for $0 < x < 1.06$. (b) Zoomed-in PXRD pattern highlighting the shifting of the $0\ 0\ 1\ 2$ and $0\ 1\ 7$ PXRD peaks of the $\text{Pb}_x\text{Sn}_{4-x}\text{As}_3$ series. (c) Change in lattice parameters as a function of Pb substitution in $\text{Pb}_x\text{Sn}_{4-x}\text{As}_3$. Shaded symbols show refined lattice parameters and empty symbols show lattice parameters calculated with DFT. (d) Change in unit cell volume as a function of Pb substitution in $\text{Pb}_x\text{Sn}_{4-x}\text{As}_3$.

Raman Characterization

We investigated the changes in the Raman spectrum with alloying, as this technique is one of the most important characterization methods for layered and 2D materials.³⁷ In Sn_4As_3 there are five Raman modes that are observed, and they occur at $85\ \text{cm}^{-1}$, $134\ \text{cm}^{-1}$, $143\ \text{cm}^{-1}$, $157\ \text{cm}^{-1}$, and $178\ \text{cm}^{-1}$. In general, as greater amounts of Pb are incorporated into the Sn_4As_3 structure, an increase in reduced mass causes most of the Raman peaks to shift to lower frequencies (Fig. 3a). Additionally, the intensity of all modes decreases with greater Pb incorporation, as would be expected when considering the reduction in polarizability and presence of local dipole moments that occur when Sn is replaced with Pb.

A polarized Raman study of the two end members of this alloy series (Sn_4As_3 and $\text{Pb}_{1.06}\text{Sn}_{2.94}\text{As}_3$) was performed to elucidate the symmetries of the Raman modes observed in this alloy series (Fig. 3b and 3c). Sn_4As_3 belongs to the $R\bar{3}m$ space group, with 4 Sn atoms and 3 As atoms each occupying a 3a Wyckoff site with local C_{3v} symmetry. Therefore, there should be a total of 14 Raman-active vibrational modes in the back-scattering measurement geometry: seven E modes and seven A_1 modes.³⁸ As Pb is alloyed into this Sn_4As_3 structure, the non-

centrosymmetric $R3m$ crystal structure transitions to a centrosymmetric $R-3m$ crystal structure. In this new $R-3m$ structure, Sn(1), Sn(2), and As(1) occupy 6c Wyckoff sites with C_{3v} symmetry while As(2) occupies a 3b Wyckoff site with D_{3d} symmetry. As a result, Sn(1), Sn(2), and As(1) each give rise to one Raman-active E_g mode and one Raman-active A_{1g} mode for a total of six Raman-active modes. The D_{3d} symmetry of As(2) does not permit any Raman-active vibrational modes.

Five Raman modes appear above 60 cm^{-1} , which is the lowest energy that our instrument can detect. In this backscattering geometry, the irreducible representation of the Raman mode is distinguished by comparing the intensity of the scattered light at different polarizations relative to the incoming laser. The E ($R3m$) and E_g ($R-3m$) modes are visible regardless of the polarization of the scattered light due to the 2-fold degeneracy along the two in-plane crystalline directions. On the other hand, the A_1 ($R3m$) and A_{1g} ($R-3m$) modes are visible in the parallel polarization configuration (0° or "XX"), but are expected to significantly decrease in intensity or disappear in the perpendicular polarization configuration (90° or "XY") relative to the E modes. As the polarizer is rotated from 0° to 90° , these A_1 and A_{1g} modes either completely or partially disappear from the spectrum. In both Sn_4As_3 and $\text{Pb}_{1.06}\text{Sn}_{2.94}\text{As}_3$ the Raman modes at 134 cm^{-1} , 157 cm^{-1} , and 178 cm^{-1} significantly decrease in intensity in the XY configuration, indicating that they have A_1/A_{1g} symmetry, whereas the Raman modes at 85 cm^{-1} and 143 cm^{-1} have similar intensities across both geometries, indicating that they have E/E_g symmetry. The lowest energy mode in $\text{Pb}_{1.06}\text{Sn}_{2.94}\text{As}_3$ at 78 cm^{-1} does decrease in intensity in XY polarization. Still, the fact that this peak is very close to the instrument detection limit and the much weaker signal in this stoichiometry makes it difficult to unambiguously assign the symmetry of this mode.

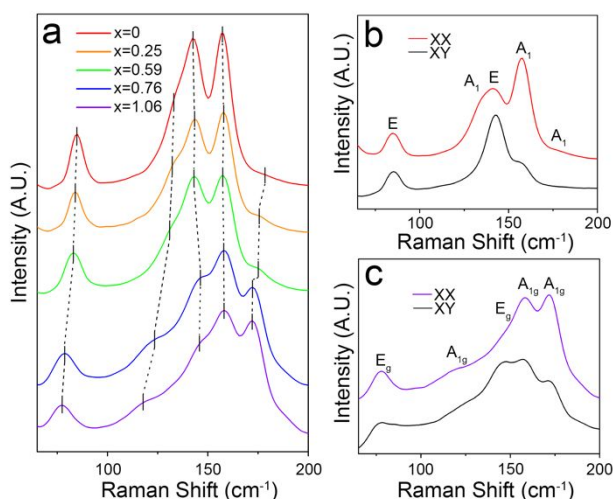


Figure 3: (a) Raman spectroscopy of the $\text{Pb}_{\text{Sn}_{4-x}\text{As}_3}$ alloy series with dashed lines to show changes in Raman shift. Polarized Raman spectroscopy of (b) Sn_4As_3 ($R3m$) and (c) $\text{Pb}_{1.06}\text{Sn}_{2.94}\text{As}_3$ ($R-3m$)

Electronic Transport

To investigate how the addition of Pb affects the electronic transport properties of the alloy series, 4-probe resistivity

measurements were conducted from 300 K to 10 K. In general, we observe that all compounds are highly metallic, having low resistivities that range from $0.48\text{ }\mu\Omega\text{ m}$ to $1.1\text{ }\mu\Omega\text{ m}$ at 300K, and that decrease with decreasing temperature (Fig. 4). In addition, the resistivity of alloys increases with greater Pb content. This increase in resistivity with greater alloy content is consistent with Nordheim's Rule.^{20–22} Substituting Sn with Pb disrupts the periodic atomic potential of the original lattice, thereby decreasing charge carrier mobility and increasing resistivity with greater alloy content. Further illustrating this point, the residual resistivity ratios of these compounds were evaluated, and found to increase with greater Pb content. Sn_4As_3 demonstrated a residual-resistivity ratio of 5.3 from 10 to 300K while $\text{Pb}_{1.06}\text{Sn}_{2.94}\text{As}_3$ demonstrated a smaller residual-resistivity ratio of 1.9. Finally, theoretical predictions of the electronic band structure of Sn_4As_3 predict it to be a metal,³⁹ as the Fermi level cuts through several bands (Fig. 5a) thereby yielding a non-zero density of states (Fig. 5b).

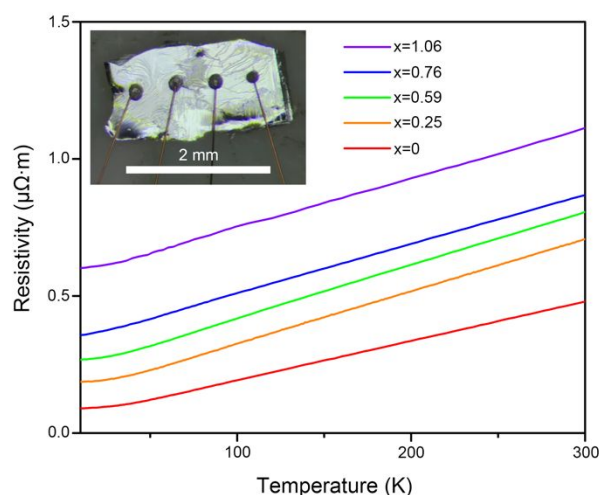


Figure 4: 4-probe resistivities of the $\text{Pb}_{\text{Sn}_{4-x}\text{As}_3}$ alloy series. The inset optical microscope image shows the setup of a 4-probe resistivity measurement on a $\text{Pb}_{1.06}\text{Sn}_{2.94}\text{As}_3$ crystal.

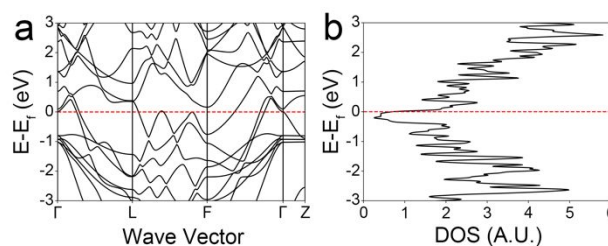


Figure 5: (a) Band structure and (b) density of states of Sn_4As_3 .

Next, we wanted to investigate the possibility of axis-dependent conduction polarity in these materials, as other layered SnAs compounds NaSn_2As_2 and NaSnAs both exhibit this effect. The in-plane and cross-plane Seebeck coefficients and the resistivities of the two end members of this alloy series, Sn_4As_3 and $\text{Pb}_{1.06}\text{Sn}_{2.94}\text{As}_3$, were measured from 80–300K (Fig. 6a and 6b). Overall, both compounds had positive Seebeck coefficients that were similar in magnitude, with the same positive sign along the in-plane and cross-plane directions. In addition, the cross-plane resistivities for both compounds were

higher than the in-plane resistivities. At 300 K, Sn_4As_3 has an in-plane thermopower of $9.6 \mu\text{V/K}$ and an in-plane resistivity of $0.34 \mu\Omega \text{ m}$ while $\text{Pb}_{1.06}\text{Sn}_{2.94}\text{As}_3$ demonstrates a similar in-plane thermopower of $12.7 \mu\text{V/K}$ and a higher in-plane resistivity of $0.98 \mu\Omega \text{ m}$. The Sn_4As_3 in-plane thermopower is relatively close to a previously reported value of $5 \mu\text{V/K}$.³³ In the cross-plane direction, both end members have a smaller thermopower ($6.2 \mu\text{V/K}$ for Sn_4As_3 and $3.9 \mu\text{V/K}$ for $\text{Pb}_{1.06}\text{Sn}_{2.94}\text{As}_3$) compared to the in-plane direction. Additionally, for both compounds, the cross-plane resistivities ($5.3 \mu\Omega \text{ m}$ for Sn_4As_3 and $6.7 \mu\Omega \text{ m}$ for $\text{Pb}_{1.06}\text{Sn}_{2.94}\text{As}_3$, at 300 K) are almost an order of magnitude larger than the in-plane resistivities, as is very common for layered materials with weaker interlayer interactions. Finally, the in-plane thermal conductivity was measured at 300 K for both compounds to be $13.0 \text{ W m}^{-1} \text{ K}^{-1}$ for Sn_4As_3 and $6.1 \text{ W m}^{-1} \text{ K}^{-1}$ for $\text{Pb}_{1.06}\text{Sn}_{2.94}\text{As}_3$. Addition of Pb into the Sn_4As_3 structure introduced alloy phonon scattering, causing the expected and observed decrease in thermal conductivity.⁴⁰

The measured 300 K Seebeck coefficient tensors are close to those predicted from the electronic band structure, assuming an isotropic scattering time approximation as implemented in the linear Boltzmann equation solver BoltzTraP. The predicted in-plane and cross-plane 300 K Seebeck coefficients for Sn_4As_3 as a function of doping are shown in Fig. 6c. Undoped Sn_4As_3 is predicted to have in-plane and cross-plane Seebeck coefficients of 16 and $7 \mu\text{V/K}$, respectively, which are within a factor of 2x of the observed values of 9.6 and $5 \mu\text{V/K}$, respectively. These calculations confirm the absence of axis-dependent conduction polarity in Sn_4As_3 when undoped, but also suggest that positive in-plane and negative cross-plane Seebeck coefficients can be achieved when the Fermi level is shifted higher by $E-E_F=0.08-0.22 \text{ eV}$. This range in doping would correspond to a sample that has been doped with $\sim 0.05-0.14$ additional electrons per Sn atom.

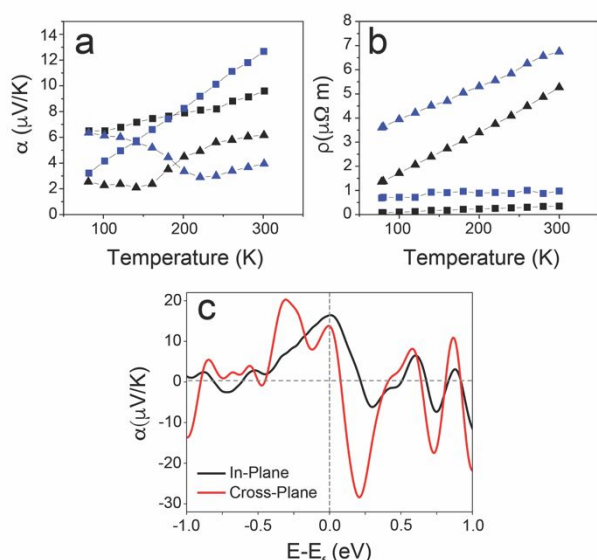


Figure 6: (a) Experimental in-plane and cross-plane thermopowers for the two end-members of the alloy series. (b) Experimental in-plane and cross-plane resistivities of Sn_4As_3 and $\text{Pb}_{1.06}\text{Sn}_{2.94}\text{As}_3$. Black markers denote Sn_4As_3 while blue markers denote $\text{Pb}_{1.06}\text{Sn}_{2.94}\text{As}_3$, and squares represent data gathered in the in-plane direction while

triangles represent data gathered in the cross-plane direction. (c) Predicted 300K in-plane and cross thermopower for Sn_4As_3 at different $E-E_F$ values.

Conclusions

In conclusion, we created a new family of layered $\text{Pb}_x\text{Sn}_{4-x}\text{As}_3$ compounds and confirmed their structure and Pb-ordering effects by DFT calculations. As Pb is alloyed into the Sn_4As_3 structure, the material undergoes a change in symmetry from $R3m$ to $R-3m$. A maximum of 25% of the Sn atoms in the Sn_4As_3 structure could be replaced by Pb atoms, forming a pseudo-binary Pb-As compound with Pb-As bonds. The Pb preferentially occupies the two central Sn sites within each Sn_4As_3 packet, leading to systematic increases in unit cell size and volume and decreases in Raman shift energies. These compounds are metallic with increasing resistivity with greater Pb alloying, which is consistent with the Nordheim rule. In contrast to other layered Sn-As materials that exhibit axis-dependent conduction polarity, small positive thermopowers were observed in both the in-plane and cross-plane directions, which is consistent with first-principles calculations. Overall, this work shows that new layered materials can be created via alloying and further illustrates that careful consideration of the electronic structure is needed to realize axis-dependent conduction polarity in new materials.

Conflicts of interest

There are no conflicts to declare.

Acknowledgements

Primary funding for this work was provided by AFOSR project no. FA9550-18-1-0335. Computations were performed on the machines of the Ohio Supercomputer Center under project no. PAS0072.

Notes and references

- 1 S. M. Young, S. Manni, J. Shao, P. C. Canfield and A. N. Kolmogorov, *Phys. Rev. B*, 2017, **95**, 1–8.
- 2 K. Lee, S. Kamali, T. Ericsson, M. Bellard and K. Kovnir, *Chem. Mater.*, 2016, **28**, 2776–2785.
- 3 H. He, R. Stearrett, E. R. Nowak and S. Bobev, *Eur. J. Inorg. Chem.*, 2011, **8**, 4025–4036.
- 4 M. Q. Arguilla, N. D. Cultrara, Z. J. Baum, S. Jiang, R. D. Ross and J. E. Goldberger, *Inorg. Chem. Front.*, 2017, **4**, 378–386.
- 5 H. Li, S. Y. Gao, S. F. Duan, Y. F. Xu, K. J. Zhu, S. J. Tian, J. C. Gao, W. H. Fan, Z. C. Rao, J. R. Huang, J. J. Li, D. Y. Yan, Z. T. Liu, W. L. Liu, Y. B. Huang, Y. L. Li, Y. Liu, G. Bin Zhang, P. Zhang, T. Kondo, S. Shin, H. C. Lei, Y. G. Shi, W. T. Zhang, H. M. Weng, T. Qian and H. Ding, *Phys. Rev. X*, 2019, **9**, 041039.
- 6 X. Gui, I. Pletikoscic, H. Cao, H. J. Tien, X. Xu, R. Zhong, G.

- Wang, T. R. Chang, S. Jia, T. Valla, W. Xie and R. J. Cava, *ACS Cent. Sci.*, 2019, 900–910.
- 7 M. Imai, K. Nishida, T. Kimura and H. Abe, *Appl. Phys. Lett.*, 2002, **80**, 1019–1021.
- 8 M. J. Evans, Y. Wu, V. F. Kranak, N. Newman, A. Reller, F. J. Garcia-Garcia and U. Häussermann, *Phys. Rev. B - Condens. Matter Mater. Phys.*, 2009, **80**, 064514.
- 9 B. He, Y. Wang, M. Q. Arguilla, N. D. Cultrara, M. R. Scudder, J. E. Goldberger, W. Windl and J. P. Heremans, *Nat. Mater.*, DOI:10.1038/s41563-019-0309-4.
- 10 M. Q. Arguilla, J. Katoch, K. Krymowski, N. D. Cultrara, J. Xu, X. Xi, A. Hanks, S. Jiang, R. D. Ross, R. J. Koch, S. Ulstrup, A. Bostwick, C. Jozwiak, D. W. McComb, E. Rotenberg, J. Shan, W. Windl, R. K. Kawakami and J. E. Goldberger, *ACS Nano*, 2016, **10**, 9500–9508.
- 11 A. M. Ochs, P. Gorai, Y. Wang, M. R. Scudder, K. Koster, C. E. Moore, V. Stevanovic, J. P. Heremans, W. Windl, E. S. Toberer and J. E. Goldberger, *Chem. Mater.*
- 12 Y. Wang, K. G. Koster, A. M. Ochs, M. R. Scudder, J. P. Heremans, W. Windl and J. E. Goldberger, *J. Am. Chem. Soc.*, 2020, **142**, 2812–2822.
- 13 M. R. Scudder, B. He, Y. Wang, A. Rai, D. G. Cahill, W. Windl, J. P. Heremans and J. E. Goldberger, *Submitted*.
- 14 Y. Tang, B. Cui, C. Zhou and M. Grayson, *J. Electron. Mater.*, 2015, **44**, 2095–2104.
- 15 M. Grayson, Q. Shao, B. Cui, Y. Tang, X. Yan and C. Zhou, in *Bringing Thermoelectricity into Reality*, 2018, pp. 81–100.
- 16 K. Schäfer, C. Benndorf, H. Eckert and R. Pöttgen, *Dalt. Trans.*, 2014, **43**, 12706–12710.
- 17 F. Gascoin and S. C. Sevov, *Inorg. Chem.*, 2002, **41**, 2820–2825.
- 18 M. T. Klem and J. D. Corbett, *Inorg. Chem.*, 2004, **43**, 5501–5504.
- 19 K. Schäfer, K. Köhler, F. Baumer, R. Pöttgen and T. Nilges, *Z. Naturforsch.*, 2016, **71**, 603–609.
- 20 B. W. Y. Redemann, M. R. Scudder, D. Weber, Y. Wang, W. Windl and J. E. Goldberger, *Inorg. Chem. Front.*, 2020, 2833–2839.
- 21 A. E. Asch and G. L. Hall, *Phys. Rev.*, 1963, **132**, 1047–1057.
- 22 G. L. Hall, *Phys. Rev.*, 1959, **116**, 604–605.
- 23 B. H. Toby and R. B. Von Dreele, *J. Appl. Cryst.*, 2013, **46**, 544–549.
- 24 G. M. Sheldrick, *Acta Crystallogr. A*, 2007, **64**, 112–122.
- 25 G. M. Sheldrick, *Acta Crystallogr. A*, 2015, **71**, 3–8.
- 26 G. M. Sheldrick, *Acta Crystallogr. C*, 2015, **71**, 3–8.
- 27 G. Kresse, *J. Non. Cryst. Solids*, 1995, **192–193**, 222–229.
- 28 G. Kresse and J. Hafner, *Phys. Rev. B*, 1994, **49**, 14251–14269.
- 29 J. P. Perdew, K. Burke and M. Ernzerhof, *Phys. Rev. Lett.*, 1996, **77**, 3865–3868.
- 30 P. E. Blöchl, *Phys. Rev. B*, 1994, **50**, 17953–17979.
- 31 G. K. H. Madsen and D. J. Singh, *Comput. Phys.*, 2006, **175**, 67–71.
- 32 S. Grimme, J. Antony, S. Ehrlich and H. Krieg, *J. Chem. Phys.*, 2010, 154104.
- 33 V. P. Eckerlin and W. Kischio, *Zeitschrift für Anorg. und Allg. Chemie*, 1968, **363**, 1–9.
- 34 K. Kovnir, Y. V. Kolen'ko, A. I. Baranov, I. S. Neira, A. V. Sobolev, M. Yoshimura, I. A. Presniakov and A. V. Shevelkov, *J. Solid State Chem.*, 2009, **182**, 630–639.
- 35 A. R. Denton and N. W. Ashcroft, *Phys. Rev. A*, 1991, **43**, 3161–3164.
- 36 L. Vegard, *Z. Phys.*, 1921, **5**, 17–26.
- 37 M. Q. Arguilla, N. D. Cultrara, M. R. Scudder, S. Jiang, R. D. Ross and J. E. Goldberger, *J. Mater. Chem. C*, 2017, **5**, 11259–11266.
- 38 M. I. Aroyo, A. Kirov, C. Capillas, J. M. Perez-Mato and H. Wondratschek, *Acta Crystallogr. Sect. A Found. Crystallogr.*, 2006, **62**, 115–128.
- 39 C. A. Marques, M. J. Neat, C. M. Yim, M. D. Watson, C. Heil, K. S. Pervakov, V. A. Vlasenko, V. M. Pudalov, A. V. Muratov, T. K. Kim and P. Wahl, *New J. Phys*, 2020, **22**, 063049.
- 40 K. Biswas, J. He, I. D. Blum, C. I. Wu, T. P. Hogan, D. N. Seidman, V. P. Dravid and M. G. Kanatzidis, *Nature*, 2012, **489**, 414–418.